Long-term creep behavior of timber columns: Experimental and numerical protocols

Frédéric Dubois, Jérôme Dopeux, Octavian Pop, Mickaël Metrope

Long-term creep behavior of timber columns: Experimental and numerical protocols

Frédéric Dubois

Univ. Limoges, GC2D, UR 14477, F-19300 Egletons, France, frederic.dubois@unilim.fr

Jérôme Dopeux

Univ. Limoges, GC2D, UR 14477, F-19300 Egletons, France, jerome.dopeux@unilim.fr

Octavian Pop

Univ. Limoges, GC2D, UR 14477, F-19300 Egletons, France, ion-octavian.pop@unilim.fr

Mickaël Metrope

Univ. Limoges, GC2D, UR 14477, F-19300 Egletons, France, mickael.metrope@unilim.fr

Corresponding author: Frédéric Dubois, e-mail: frederic.dubois@unilim.fr, Phone: (+33) 6 31 25 27 90, Tel: (+33) 5 55 93 45 25

Abstract

This work deals with an experimental and numerical approach to determining the differed behavior of compressed wood elements subjected to creep loading. An experimental protocol is associated with a mechanical model, whose purpose is to isolate the effects of creep from those of shrinkage-swelling, while allowing for a long duration test to be conducted. The experimental protocol is based on a compression creep test applied to five wooden columns disposed in a climatic room for one year. The numerical model is based on the use of a Kelvin-Voigt rheological model associated with a shrinkage-swelling element. An optimization study is proposed in order to interpolate the model parameters with respect to the experimental measurements. In the context of a linear viscoelastic behavior, the result of this interpolation allows to propose a model extrapolation for long times. Within the framework of the European code, Eurocode 5, this project aims to identify the long-term creep coefficient (kdef) adapted to compressed elements, in addition to evaluating the partial creep coefficients as a function of loading duration class.

Keywords: Compression creep, Viscoelastic behavior, Spectrum decomposition, Creep extrapolation, Eurocodes

Acknowledgments: The authors would like to thank the *AdivBois* association 'Association for the Development of Timber Living Buildings' for funding this study. This work was carried out within the framework of the study on high-rise timber buildings. Given this context, the authors also express their gratitude to the Timber Construction Technology Platform for facilitating the technical execution of this study.

1. Introduction

Today, wood is one of the materials of the future in civil engineering because it is natural and it requires low consumption of fossil resources. Moreover, timber constructions store carbon dioxide which is the major cause of

climate change. Finally, wood is often a local material that enhances short circuits by limiting the environmental impact in terms of transport. Thus, many countries and regions, with their abundant forest resources, attach considerable importance to the use of this resource in construction by considering wood as an economical and efficient structural material. Today, many technological and scientific challenges are proposed to realize timber road bridges or high-rise buildings beyond ten floors. These new structures require the completion of regulatory texts in order to adapt them to these new constructions.

In recent years, several experimental and numerical studies have been carried out to investigate the use of structural wood elements in the construction of high-rise buildings or large-span structure. In order to increase the resistance of these construction elements, most of these studies propose reinforcement solutions. Concerning large-span structures Xu et al. [1] propose an interesting study, using the L shaped column fabricated using Steel-Timber Composites (STC). The study demonstrated that for axial compression the L-STC columns stiffness and load-carrying capacity are enhanced in comparison with CLT or Glue Laminated elements. Kang et al. [2] have also studied the strength capacity, stiffness, ductility, energy dissipation and equivalent damping ratio glulam timber frames under reversed cyclic loading conditions. The study showed that the seismic behavior is significantly enhanced by using top-and-seat steel-angle connections and diagonal braces. O'Callaghan et al. [3] show that in the case of square timber columns wrapped with fiber-reinforced polymer (FRP) composites under compression loading, a proper thickness of FRP wrapping can prevent undesirable failures and reduce the influence of naturally defects of wood. For Cross-Laminated Timber (CLT) elements subjected to blast loads, Lopez-Molina and Doudak [4] show that reinforcing the panels with steel straps had minimal effect on the ultimate strength, but significantly affected the post-peak resistance and ductility. The whole of these works relates more particularly to the strength capacity of the carrying elements.

In high-rise buildings, vertical supports such as columns are typically subjected to compression or compound bending loads. If, today, some works have been done on the axial and transverse compressive strength [5], few studies have focused on the differed deformation behavior. In this context, Jockwer et al. [6] proposed an experimental monitoring of the short and long term deformation behavior of highly loaded components. This work is based on a monitoring approach of the vertical carriers. It highlights the difficulty of separating the different effects induced by a complex mechanical behavior coupling viscoelasticity, shrinkage and swelling caused by moisture variations and mechanosorptive effects. In a similar way to the consideration of deferred effects on bent structures, the deferred deformations can be parameterized by a creep coefficient balanced by a service class related

to the external environment. But moreover, the effects of shrinkage-swelling must be controlled, which is not the case today for bent elements.

Considering the effects of creep on the long-term behavior of wood structures is nowadays a necessity for both bending and compression elements. The European regulation Eurocode 5 [7] integrates this notion only in the case of the calculation of the deflection of bending elements and in the long-term stiffness of fasteners. This consideration has been reflected by an amplification of the deflections through a coefficient k_{def} modulated by the duration of the given loading and service class. In the context of developing high-rise structures, the vertical carriers play a predominant mechanical role. At the serviceability limit state, the cumulative compressive deformation generates vertical displacements that can no longer be ignored or neglected. Currently, design engineers use creep coefficients determined on the basis of bending due to a lack of guidance from the Eurocode. In addition, structural elements are subject to dimensional variations as a result of drying and wetting kinetics. While in bending parts, these effects do not significantly contribute to the variations and changes in deflection, such is no longer the case for compressed elements whose effects are proportional to the height of vertical supports. Therefore, with respect to high-rise buildings beyond ten floors, these effects can no longer be neglected.

However, the compressed load-bearing elements are dimensioned with large cross-sections (1m x 1m for instance). In contrast to bent elements, the compressive stress is distributed evenly over the entire cross-sectional area. Under these conditions, the creep effects are evenly distributed over the entire resisting section. Moreover, the size of transversal sections induces important inertia effects in terms of moisture transfer. If it is important to consider moisture content variations between the manufacturing area of the elements, their storage places and their final destination in the building, the humidity variations induced by a service class 1 (in heated or air-conditioned interior), will not generate representative hydric disturbances on the whole of the cross sections. For this reason, this work focuses on the characterization of the creep behavior in a climatic chamber at constant temperature and relative humidity.

At the local scale, in assuming a linear viscoelastic behavior combined with swelling-shrinkage effects, mechanical behavior is defined as the relationship between stresses $\sigma(t)$ and strains $\varepsilon(t)$. According to a unidimensional approach, this mechanical behavior is defined by the following expression [8] [9] [10]:

$$\varepsilon(t) = \int_{t_o}^{t} J(t-\tau) \cdot \frac{\partial \sigma}{\partial \tau} d\tau + \alpha \cdot \left(w(t) - w(t_o) \right) \qquad (1)$$

where $J(t)$ is the creep function. According to a uniaxial approach, the effects of shrinkage-swelling are taken into account by considering the differential variation between moisture content $w(t)$ at time t and the reference moisture content state $w(t_o)$ at the initial time t_o, which corresponds to the loading time. In this formulation, the shrinkage-swelling coefficient is denoted α. By adapting this global expression to a creep condition and then employing the generalized stresses used in beam theory, Eq. (1) can be rewritten as follows:

$$u_{fin}(t) = h_o \cdot \frac{J(t-t_o)}{S} \cdot F_o + h_o \cdot \alpha \cdot \left(w(t) - w(t_o)\right) \quad (2)$$

in which $u_{fin}(t)$ is the relative displacement of the column head, S the cross-sectional area, h_o the initial column height, and F_o the creep constant force. This work does not address the entire problem but instead focuses on determining the k_{def} coefficient for compressed elements.

To proceed, a first section will detail the materials and methods by presenting the creep experimentation that entails a creep test bench adapted to compressed elements.

Since compressed columns are placed in a climate-controlled chamber after several days of conditioning, the prediction of moisture content evolution needs to be evaluated. A numerical approach, optimized with experimental measurements, will be presented in the second section in order to separate the swelling-shrinkage effects from the creep response.

As such, to correct the first instants of creep from the shrinkage-swelling effects, a creep recovery protocol will be developed in the third section.

The last section will discuss the final analysis of the experimental data in the aim of determining the long-term behavior of the compressed elements by means of extrapolating the experimental results to 50 years of creep response. This extrapolation allows setting the new value of k_{def} and offering an assessment of the results obtained.

2. Materials and methods

2.1.Experimental set-up

The experimental equipment used herein has been based on an experimental creep device capable of handling five glue laminated spruce columns. To limit the risk of instability, specimen height is limited to 75cm and its cross-section is set at 100 x 200mm² corresponding to a slenderness ratio λ of 26 in the week direction. The cross section is composed of 5 lamellae whose growth rings are also visible on the Fig. 1.

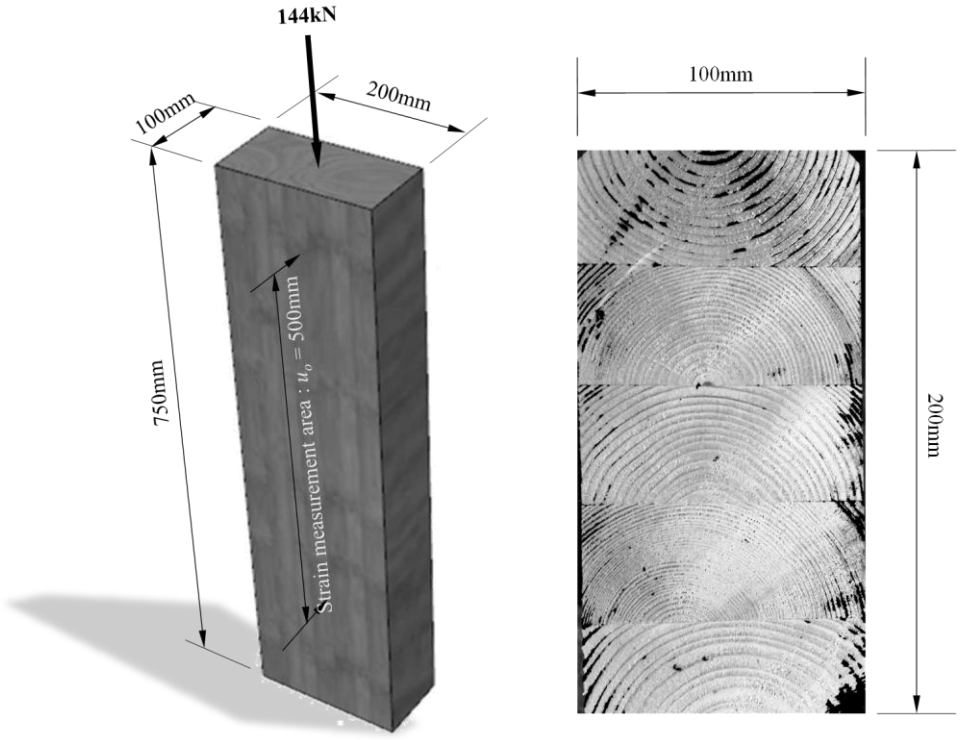

Fig. 1 Specimen geometry

Given that the definition of creep requires measuring the axial strain, a 500mm long zone is identified in bypassing the set of boundary condition problems. In this case, the local strain is calculated with the relative displacement Δu, as measured in this area in accordance with the following expression:

$$\varepsilon = \frac{\Delta u}{h_o}, \; with \; h_o = 500mm \tag{3}$$

Δu is measured by using the mean of two resistive displacement sensor responses placed in the front and back of the specimen faces, as shown in Fig. 2.

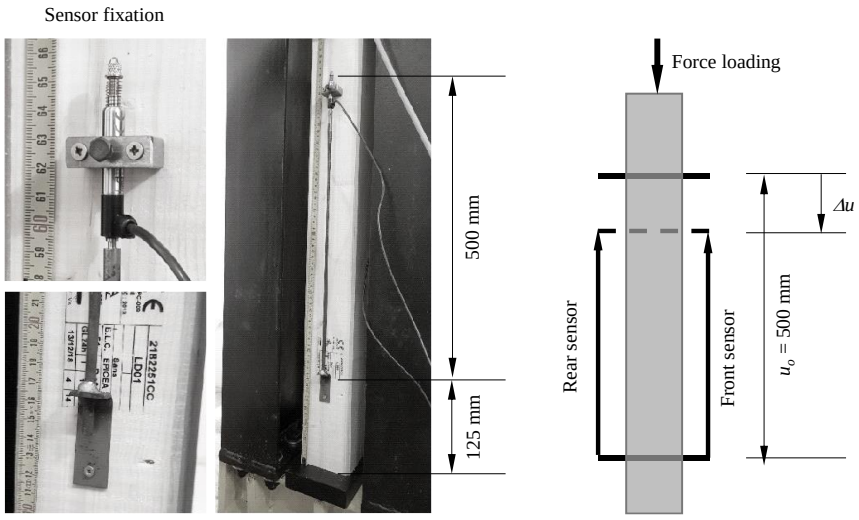

Fig. 2 Strain measurement device

Based on the mechanical strength class, the stress state is limited to 30% of the ultimate limit state compression value of 7.2MPa, which corresponds to an axial force loading of 144kN for each specimen. This force loading is adjusted by the system's three screws. The device design has been enhanced to obtain an acceptable stiffness relative to the experimental specimens, Fig. 3.

Fig. 3 Experimental creep device

Given that a creep state necessitates a controlled and homogeneous stress distribution, a distribution plate is placed between a force sensor and the column head. The loading device is presented in Fig. 4. In searching for a homogeneous distribution of internal moisture, as opposed to the work conducted on CLT creep proposed by Gräfe et al. [11] [12], we have opted to lay the columns out horizontally so as to generate identical thermal and hydric convective exchanges on all four faces. Moreover, the enclosure has been equipped with fans that allow stirring the air and controlling exchange conditions on the surface.

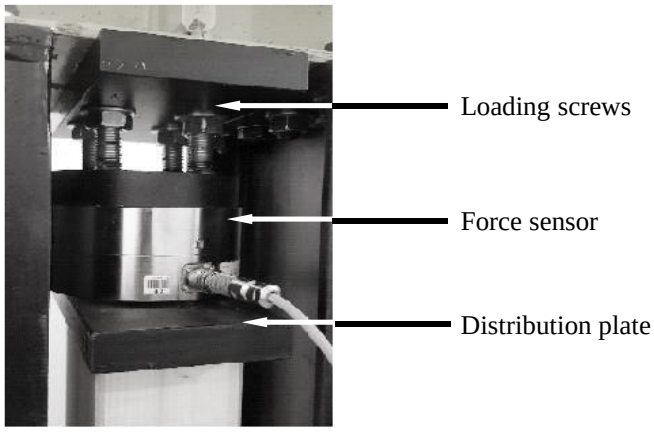

Fig. 4 Loading system principle

In accordance with service class no. 1, the experimental device is to be placed in a climate-controlled room, where the climate is controlled in terms of both temperature (20° +/- 2°C) and relative humidity (65% +/- 5% RH).

2.2 Initial moisture content distribution

Since the creep response is influenced by the temporal evolution of the moisture content, the experimental protocol requires the integration of its control. Between the moisture state during the glue laminated design of the column and subsequent installation in the climate-controlled room, it is necessary to measure the humidity state. In respecting this consideration, during specimen machining, a 2-cm thick plate was isolated, with 15 cubes 2.5 cm to a side being extracted in order to measure the local moisture constant after drying in an oven at 103°C, Fig. 5. The moisture content values are listed in Table .

S11 *10.8%*	*S21* *12.1%*	*S31* *11.9%*	*S41* *11.5%*	*S51* *10.6%*
S12 *11.3%*	*S22* *12.7*	*S32* *12.7%*	*S42* *12.6%*	*S52* *11.2%*
S13 *10.3%*	*S23* *11.3%*	*S33* *11.3%*	*S43* *10.9%*	*S53* *11.0%*

Table 1 Initial moisture content distribution in the cross-section

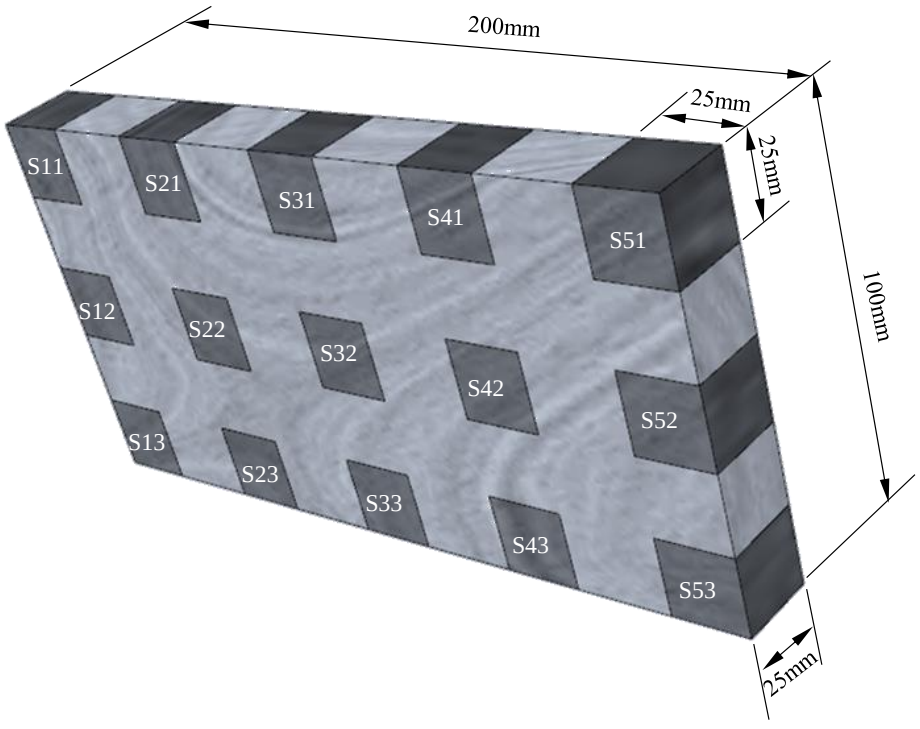

Fig. 5 Cutting of the cross section into 15 cubes

The projection of local moisture content measurements onto a finite element support allows representing a map of the moisture content distribution, as shown in Fig. 6. The moisture highlights a drying phase between the column

design time and the conditioning phase before experimental testing with a maximum deviation of 3% between the core and periphery of the specimens.

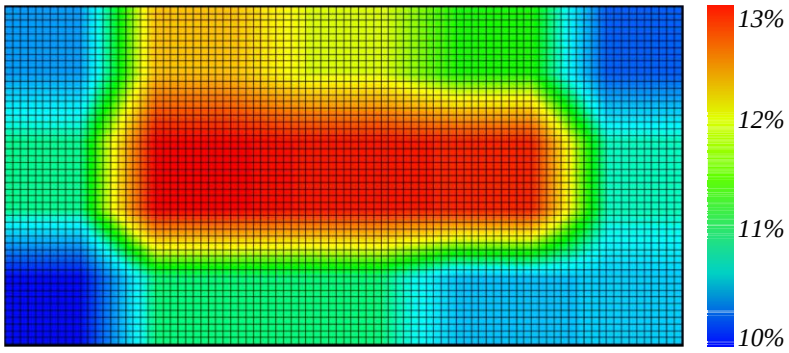

Fig. 6 Moisture content mapping in the cross-section

2.3 Creep and recovery experimentation

According to the moisture content map shown above and the updated environmental climate imposed in the climate-controlled chamber, the creep response will be made noisy by a moisture content evolution starting at its initial value w_{ini} and extending until reaching stability w_{equ}. Since a decoupling between moisture content and creep evolution is required, we have opted for a specific loading that includes both an initial creep loading during the moisture content stabilization phase and a recovery phase in a state of constant moisture content (Fig. 7).

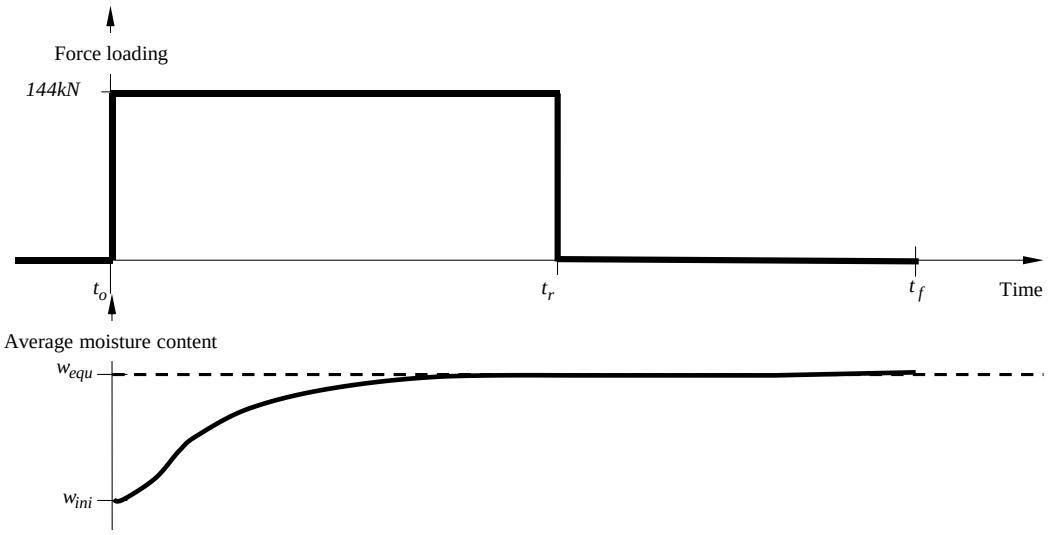

Fig. 7 Creep end recovery loadings vs. average evolution of moisture content over time

Columns are loaded at time t_o. The start of recovery is the unloading time t_r, when average moisture content has reached equilibrium. Moreover, the total experimental test time t_f comprises the total creep and recovery responses, which are necessary to approximate the long-term strain response through an extrapolation algorithm. In such a context, we have chosen specimen no. 3 to estimate all times as a function of the mass transfer kinetics

between times t_o and t_r. The final time t_f has been shortened in order to validate the moisture condition assumptions.

3. Moisture content corrections

3.1 Mass transfer simulation

The evaluation of recovery time t_r is primarily based on a mass transfer simulation by applying a nonlinear orthotropic Fick's Law through the cross-section, as described by the following equation:

$$\frac{\partial w}{\partial t} = div\left(\mathbf{D} \cdot \overrightarrow{grad}\left(w\right)\right) \tag{4}$$

where $\mathbf{D}$ denotes the second-order diffusion tensor. In the main orthotropic frame of reference, this tensor is represented by a diagonal matrix. By limiting the simulation to the cross-section characterized by the radial and tangential directions, respectively $\vec{R}$ and $\vec{T}$, the diffusion tensor can be characterized by the two following nonlinear radial and tangential diffusion coefficients:

$$D_R\left(w\right) = D_R^o \cdot \exp\left(k_R \cdot w\right) \text{ and } D_T\left(w\right) = D_T^o \cdot \exp\left(k_T \cdot w\right) \tag{5}$$

D_R^o and D_T^o are the anhydrous diffusion coefficients for the radial and tangential directions. k_R and k_T integrate a nonlinear phenomenon typically observed in wood materials. According to Manfoumbi's findings [13], spruce diffusion properties are given in Table 2.

D_R^o	D_T^o	k_R	k_T
$2.48 \cdot 10^{-10} m^2 \cdot s^{-1}$	$1.24 \cdot 10^{-10} m^2 \cdot s^{-1}$	0.25	0.25

Table 2 Diffusion properties for the spruce species

In terms of boundary conditions, the water exchanges taking place between the environmental area and the specimen surfaces are expressed via the sorption isotherm curve found in Merakeb's formulation [14], i.e.:

$$\ln\left(\frac{w_{equ}}{w_s\left(T\right)}\right) = \phi \cdot \ln\left(RH\right) \cdot \exp\left(\alpha_{RH} \cdot RH\right) \tag{6}$$

ϕ and α are two thermodynamic parameters characterizing the sorption isotherm. w_s designates the equilibrium moisture content reached for 100% RH; its value is temperature-dependent in accordance with the following expression [15]:

$$w_s\left(T\right) = \left(w_s^o + \frac{C_{anh}}{C_{pv}}\right) \cdot \exp\left(-\frac{C_{pv}}{L} \cdot T\right) - \frac{C_{anh}}{C_{pv}} \quad (T \text{ given in °C}) \tag{7}$$

Table 3 indicates the isotherm parameter values for spruce.

ϕ	α_{RH}	w_s^o	L	C_{pv}	C_{anh}
0.82	1.435	35.4%	$2500kJ \cdot kg^{-1} \cdot K^{-1}$	$4180kJ \cdot kg^{-1} \cdot K^{-1}$	$2160kJ \cdot kg^{-1} \cdot K^{-1}$

Table 3 Sorption isotherm parameters for spruce

In combining Eq. (6), (7) and the temperature and relative humidity evolutions, Fig. 8 serves to predict the average balanced moisture content at around 13.9%.

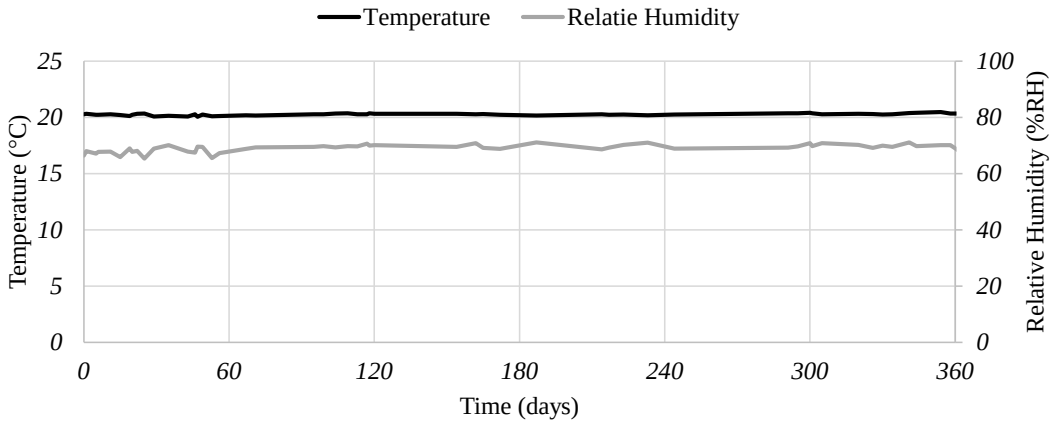

Fig. 8 One-year temperature and relative humidity variations in the climate-controlled chamber

The mass transfer algorithm implemented in the finite element software Castem is based on the mesh shown below, in considering the orthotropic reference cylinder in the radial-tangential plane with its heterogeneity being induced by the various lamellas. The isoperimetric finite element size (2 mm) and time increment (1 day) are fixed in order to ensure spatial and temporal convergence. The boundary conditions are based on an imposed and constant moisture content of 13.9% on the surface, Fig. 9.

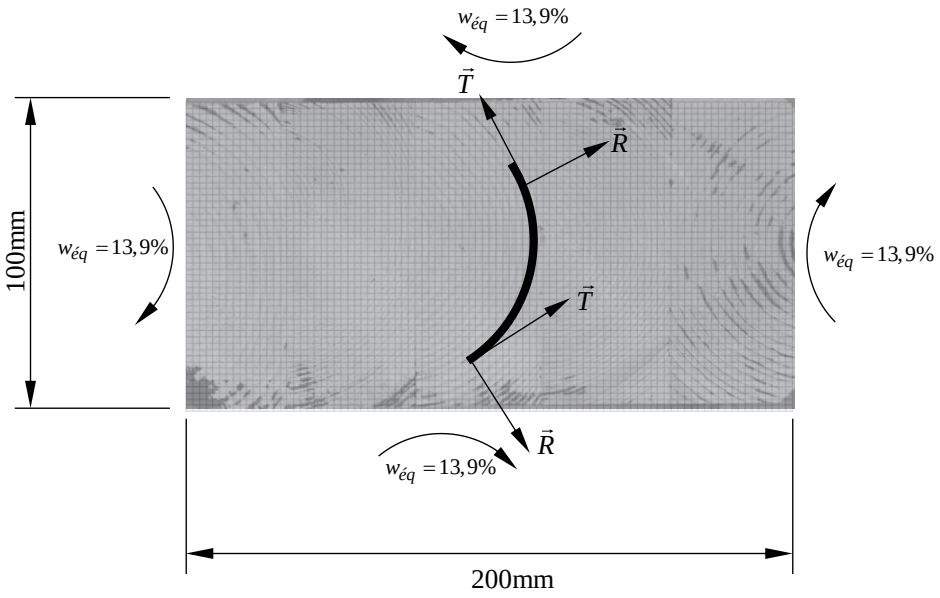

Fig. 9 Finite element mesh and boundary conditions

The initial moisture content map has been introduced as the interpolated distribution shown in Fig. 7. Moreover, the effects of convective exchanges are to be considered as an instantaneous exchange.

3.2 Moisture content evolution

The predicted time evolution of the average moisture content is plotted in Fig. 11. In terms of moisture content mapping evolution, let's note a global increase with a homogenization taking place from one day to the next. The average moisture content evolution shows stability from right around 200 days. According to the force loading principle (Fig. 10), it can be concluded that the recovery time must be set at between 200 days and one year upon completion of the force loading process. The experimental strategy employed herein focuses on a time recovery of 200 days for column no. 3. The total experimental time equals one year. At the end of the creep and recovery experimental test, the moisture content evolution was controlled by cutting three 2-cm thick plates, from which 15 cubes 2 cm to a side were placed in an oven for drying and evaluating the final moisture content map.

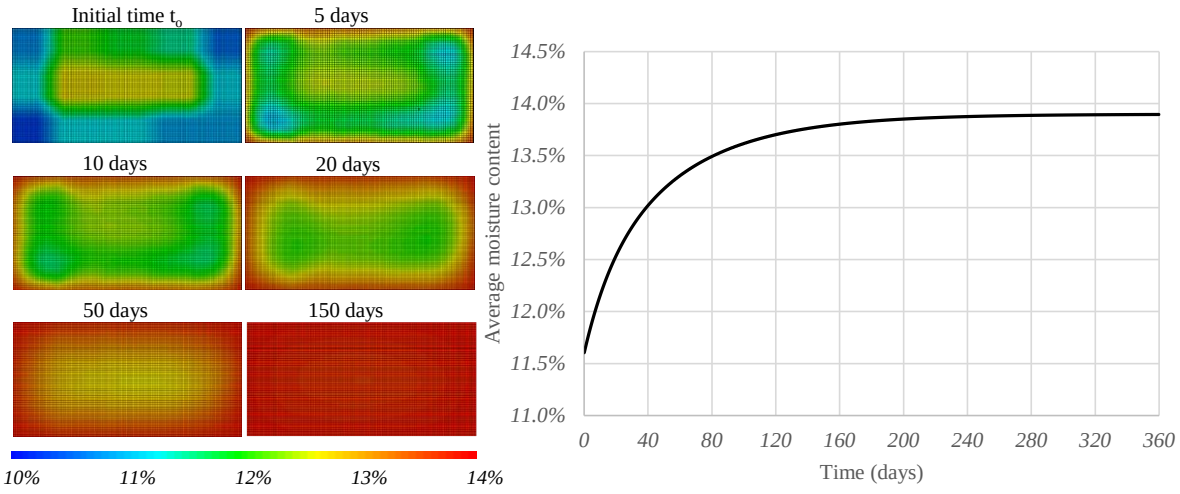

Fig. 10 Time evolution of the average moisture content and various MS maps

Lastly, the final moisture content was defined for 50 cubes, with an average value of 13.85% and a standard deviation of 0.4%, thus confirming the accuracy prediction along with a homogeneous state.

4. Creep end recovery testing

Based on specimen no. 3, this experimental test is composed of a creep phase with, in parallel, a phase of constant moisture equilibrium. This experimental protocol induces several phenomena, such as swelling effects, an impact on the axial elastic modulus and an increased creep response time. The subsequent protocol has been designed to control and isolate all these effects. For specimen no. 3, the external loading is shown in Fig. 11 for an axial stress value of 7.3 MPa. The force evolution highlights the effects of swelling at the start of loading, resulting in a slight increase in force during the first 120 days, despite the correction introduced by the experimenter.

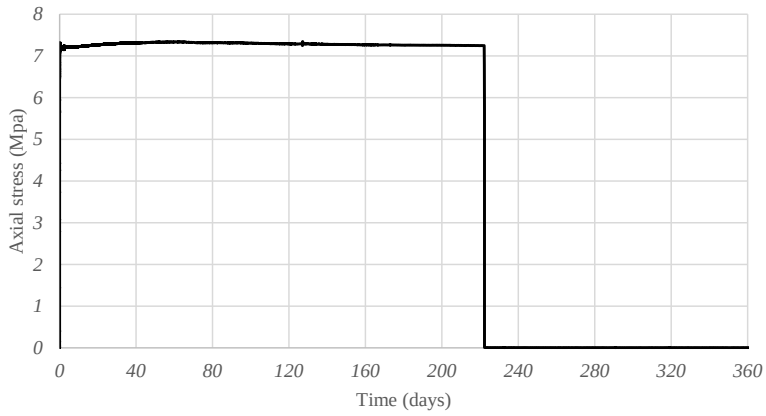

Fig. 11 Creep and recovery experiment for specimen no. 3

The recovery phase starts after 220 days. As shown in Fig. 12, the experimental protocol makes it possible to define the following four phases:

– Instantaneous elastic response at an 11.6% average moisture content during a 220-day loading phase,

– Instantaneous elastic response at a 13.9% constant moisture content during the loading phase,

– Creep behavior under an increase in moisture content,

– Recovery behavior under a constant moisture content for 140 days.

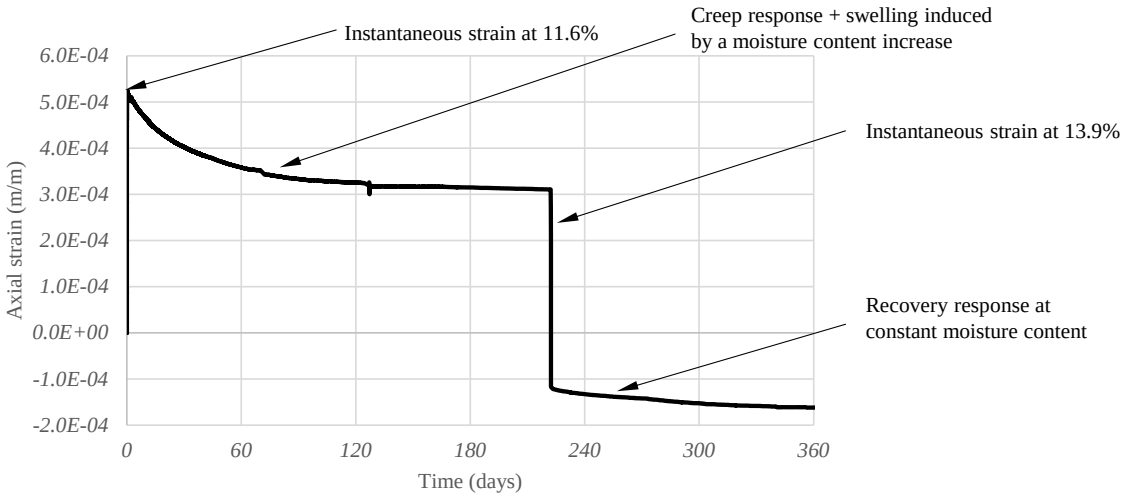

Fig. 12 Creep and recovery response

4.1 Instantaneous elastic response

The elastic modulus is evaluated by conducting a linear regression modulated by loading and unloading time, respectively. Table 4 provides the elastic modulus values for all specimen evaluated at the loading phase (at an average moisture content of 11.6%) and at the unloading time (at a moisture content of 13.9%).

Specimen number	Axial elastic modulus (GPa)	
	Loading time	Unloading time
1	14.1	13.5
2	13.9	15.1
3	14.4	13.9
4	14.3	14.6
5	15.2	15.0

Table 4 Elastic modulus measured by linear correlation during loading and unloading phases

4.2 Creep and recovery behavior under an increasing moisture content

By applying the principle of superposition, legitimized by the assumption of a linear behavior, after unloading at the time t_r, the recovery deformation admits the form deduced from the expression (1) :

$$\varepsilon(t) = \sigma_o \cdot \left(J(t - t_o) - J(t - t_r) \right) + \alpha \cdot \left(w(t) - w(t_o) \right) \tag{8}$$

The creep function $J(t)$ is normally represented by a creep spectrum, according to the following Prony series, such that:

$$J(t) = \frac{1}{E_L} \cdot \left[1 + \sum_{m=1}^{M} \chi_m \cdot \left(1 - \exp^{-\frac{t}{\tau_m}} \right) \right] \tag{9}$$

χ_m denotes the creep coefficient, in accordance with the strain kinetics coupled with characteristic times τ_m, in response to an exponential distribution. For our specific case, in considering a total experimental time of one year, let's consider the three characteristic times of one week, six months and one year ($M = 3$). In these conditions, characteristic times τ_m are calculated to have a 99% creep limit à time t_m such as :

$$\tau_m = -\frac{t_m}{\ln(1 - 0.99)} \text{ with } t_1 = 7 \text{ days}, \; t_2 = 180 \text{ days} \text{ and } t_1 = 360 \text{ days} \tag{10}$$

Finally, by regrouping the Eq. (8), (9) and (10), an optimization algorithm is used to determine the parameters χ_m and the axial shrinkage swelling coefficient α . The convergence criterion of the optimization is based on a least squares minimization of the difference between the experimental measurements and the model data over the entire experimental time range (360 days). The model parameters are given in Table 5 and the axial shrinkage swelling coefficient converges at the value of $1.13 \cdot 10^{-4}$ / % . Finally, Fig. 13 illustrates a good fit between the experimental and model creep strains.

$\tau_1(day)$	$\tau_2(day)$	$\tau_3(day)$	χ_1	χ_2	χ_3
1.52	39.1	62.1	$1.93 \cdot 10^{-3}$	$7.60 \cdot 10^{-2}$	$9.48 \cdot 10^{-2}$

Table 5 Creep spectrum properties

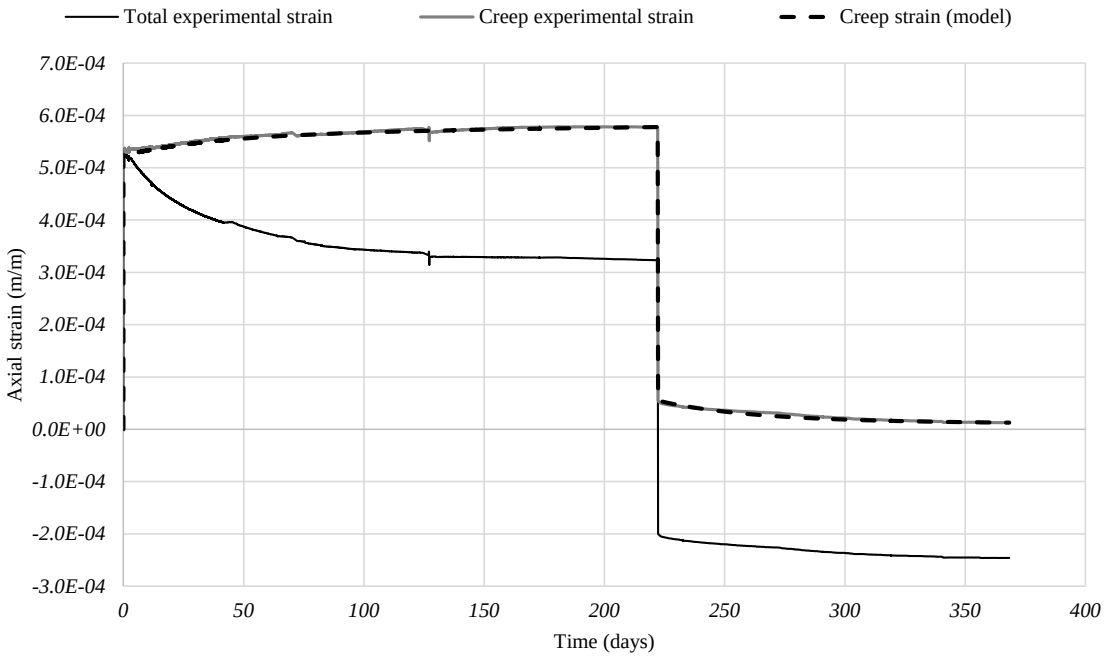

Fig. 13 Experimental and model creep strains, column n°3

Fig. 14 shows the synthetic results for the other 4 specimens. Note that the correction of the swelling effects was taken from the column n°3.

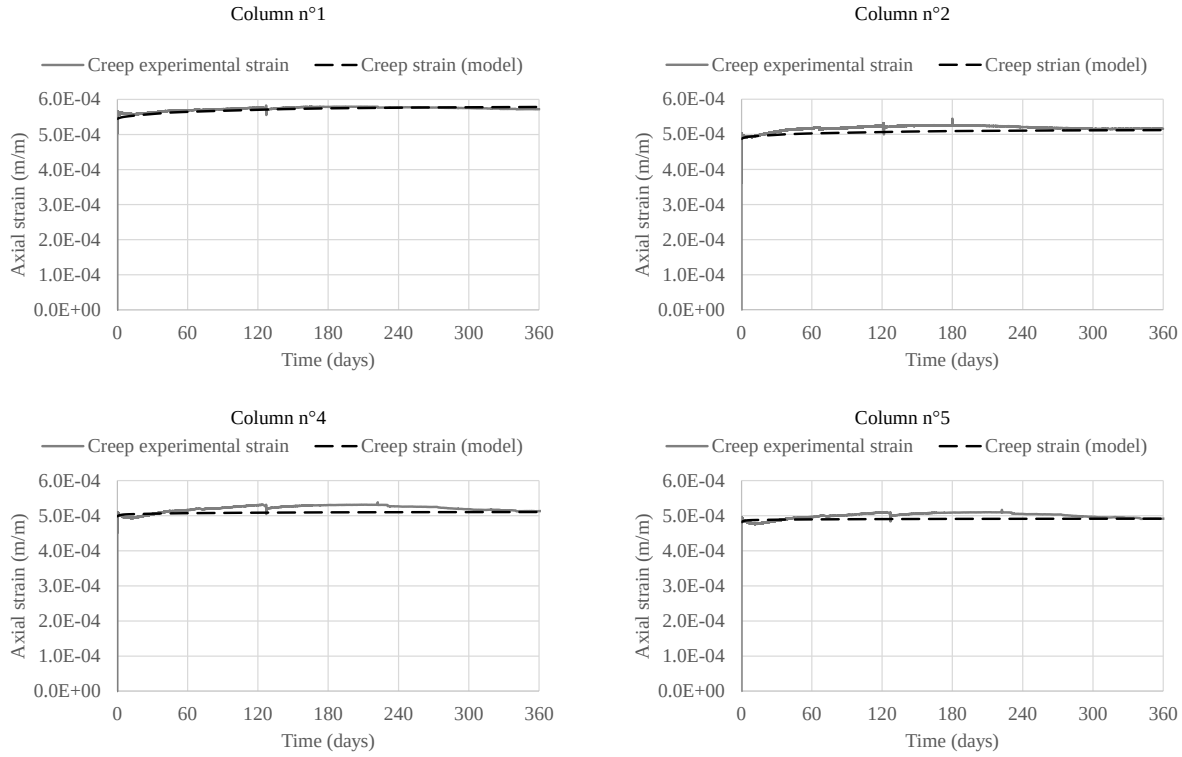

Fig. 14 Experimental and model results for samples 1, 2, 4 and 5

This fact explains the small differences between model and experiment. However, for all samples, the differences disappear after one year of creep, which will allow, in the continuation of this study, to have a good extrapolation until 50 years. In this context, we note the importance, in the future, to integrate a recovery phase after 6 months to better interpret the effects of swelling process.

4.4 Numerical extrapolation

Since long-term timber behavior must be predicted for 50 years, let's use an extrapolation method based on a property of the linear viscoelastic behavior, whereby after the first primary creep phase, the time-dependent strain adopts the following form [10], as illustrated in Fig. 15:

$$\ln\left(\varepsilon\left(t\right)\right) = a \cdot \ln\left(t\right) + b \tag{11}$$

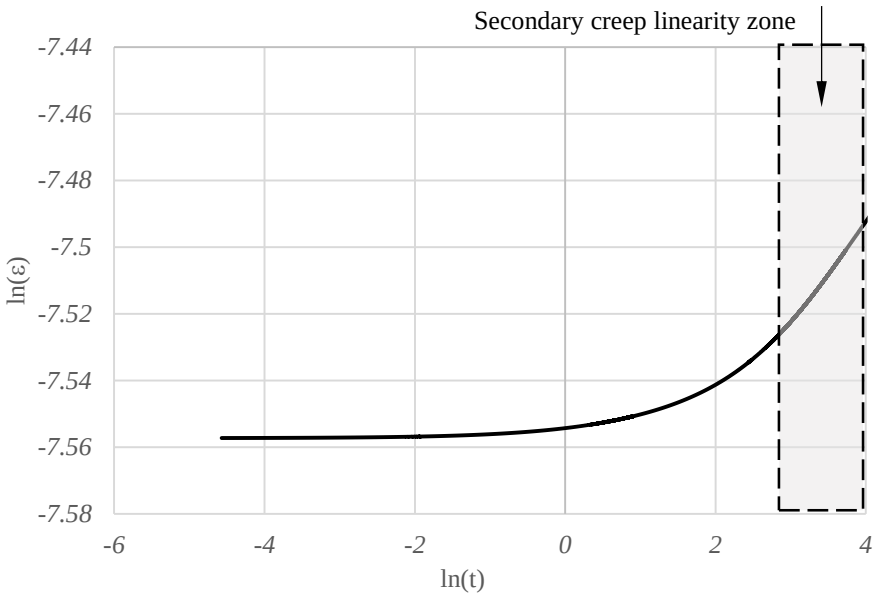

Fig. 15 Logarithmic linearity during secondary creep

For all columns, the linear correlation yields coefficients a and b, as listed in Table 8.

Column	*1*	*2*	*3*	*4*	*5*
a	$1.73 \cdot 10^{-2}$	$3.27 \cdot 10^{-2}$	$2.99 \cdot 10^{-2}$	$3.32 \cdot 10^{-2}$	$3.23 \cdot 10^{-2}$
b	7.51	7.66	7.61	7.65	7.60

Table 8 Linear correlation coefficients

Lastly, the results of this numerical extrapolation can be illustrated by Fig. 17 for one year. The results observed are encouraging in that the experimental data are sufficiently denoised by means of the interpolation method to produce an accurate creep interpolation during the loading phase, thus leading to an efficient long-term extrapolation.

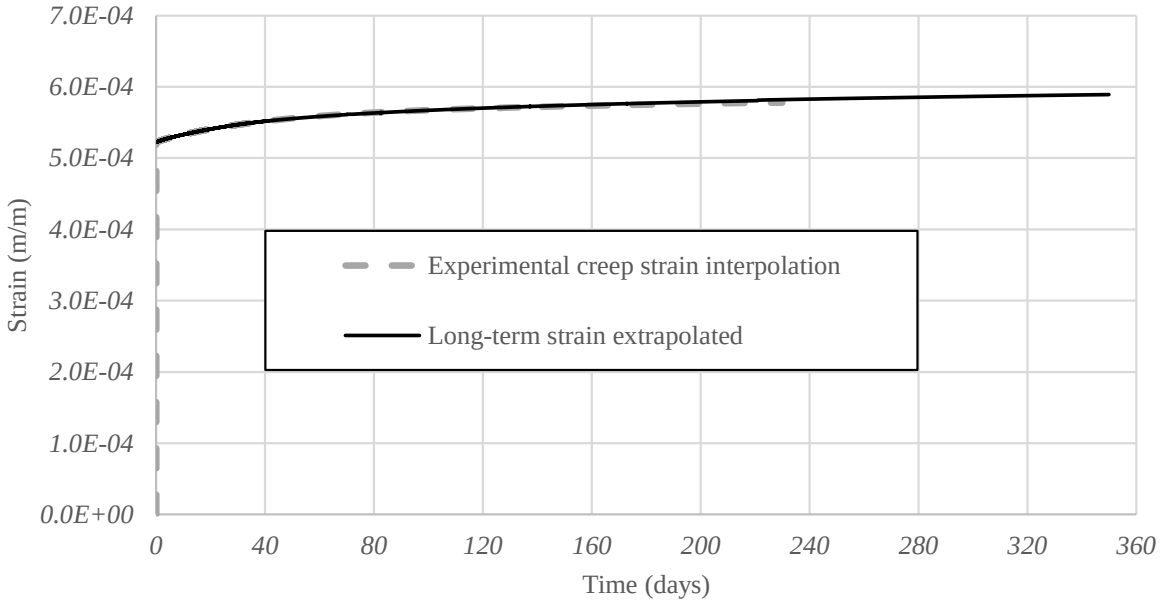

Fig. 16 Creep extrapolation results for one year (Column no. 3)

5. Differed strain

All experimental results allow for a determination of the creep strain under a constant axial stress loading. These results, completed by the approximation process, are indicated in Table 6.

Columns	*1*	*2*	*3*	*4*	*5*
$\sigma(MPa))$	7.30	7.25	7.30	7.23	7.22
$\varepsilon_{inst}\,(m/m)$	$544\cdot10^{-6}$	$487\cdot10^{-6}$	$522\cdot10^{-6}$	$499\cdot10^{-6}$	$482\cdot10^{-6}$
$\varepsilon_{six\ months}\,(m/m)$	$545\cdot10^{-6}$	$488\cdot10^{-6}$	$523\cdot10^{-6}$	$499\cdot10^{-6}$	$483\cdot10^{-6}$
$\varepsilon_{ten\ years}\,(m/m)$	$588\cdot10^{-6}$	$542\cdot10^{-6}$	$631\cdot10^{-6}$	$578\cdot10^{-6}$	$543\cdot10^{-6}$
$\varepsilon_{fifty\ years}\,(m/m)$	$632\cdot10^{-6}$	$609\cdot10^{-6}$	$662\cdot10^{-6}$	$635\cdot10^{-6}$	$622\cdot10^{-6}$

Table 6 Deferred creep strains

5.1 Spectral decomposition of creep functions

The spectral decomposition of creep allows separating the temporal spectrum by considering the loading times defined in Eurocode 5, i.e., one week, six months, ten and fifty years. Under these conditions, the creep function (10) can be rewritten as follows:

$$J(t)=\frac{1}{E_L}\cdot\left[1+\sum_{m=1}^{4}\chi_m\cdot\left(1-\exp^{-\frac{t}{\tau_m}}\right)\right] \qquad (12)$$

where E_L denotes the longitudinal elastic modulus defined for the equilibrium moisture content of 13.9%. τ_m are the characteristic times calculated based on load duration times; they have been calculated according to the following expression:

$$\tau_m = -\frac{t_m}{\ln(\xi)} \tag{13}$$

t_m is the time corresponding to the various loading times. ξ, given as a percentage, designates the activation residual of each term of the series associated with each loading duration. Its value here has been set at 1%. Also, χ_m represents the optimization parameters required to fit the experimental and extrapolated creep curves out to 50 years of loading. Fig. 18 presents the results of the optimization routine for column no. 3.

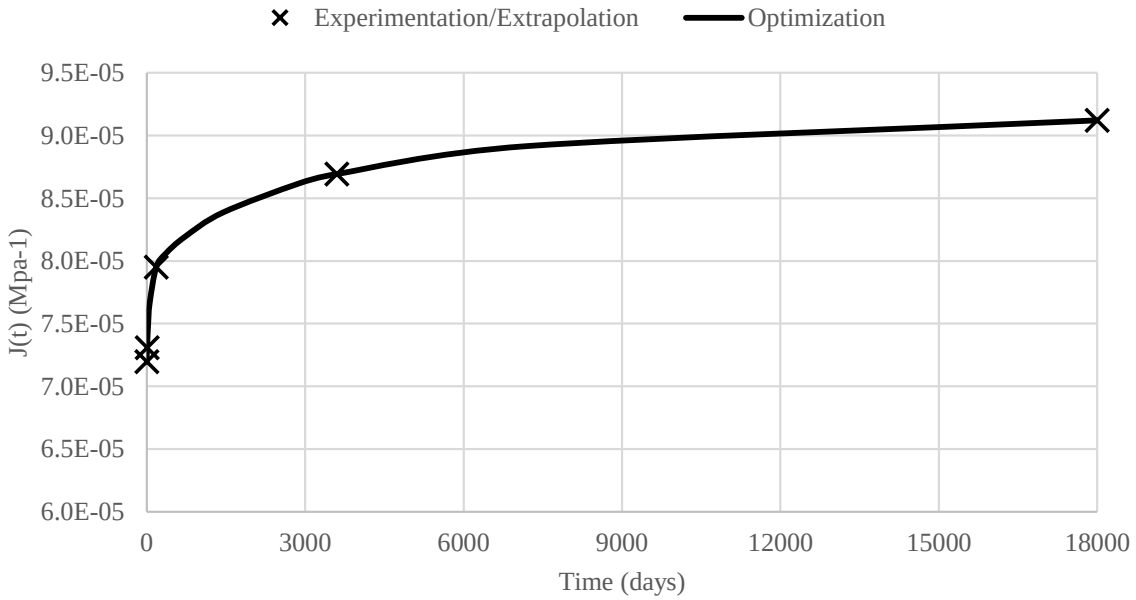

Fig. 17 Results of creep optimization (Column no. 3)

For each loading duration, the Table 7 specifies the various optimization parameters for each column.

m	*1*	*2*	*3*	*4*
t_m	*7 days*	*6 months*	*10 years*	*50 years*
τ_m *(days)*	*2.34*	*60.1*	*1,200*	*6,010*
χ_m *(Column no. 1)*	$2.46 \cdot 10^{-2}$	$3.76 \cdot 10^{-2}$	$3.65 \cdot 10^{-2}$	$5.98 \cdot 10^{-2}$
χ_m *(Column no. 2)*	$5.64 \cdot 10^{-2}$	$9.24 \cdot 10^{-2}$	$6.93 \cdot 10^{-2}$	$1.24 \cdot 10^{-1}$
χ_m *(Column no. 3)*	$5.03 \cdot 10^{-3}$	$9.32 \cdot 10^{-2}$	$6.32 \cdot 10^{-2}$	$1.13 \cdot 10^{-1}$
χ_m *(Column no. 4)*	$5.03 \cdot 10^{-3}$	$8.36 \cdot 10^{-2}$	$6.95 \cdot 10^{-2}$	$1.24 \cdot 10^{-1}$
χ_m *(Column no. 5)*	$6.95 \cdot 10^{-2}$	$6.79 \cdot 10^{-2}$	$7.32 \cdot 10^{-2}$	$1.32 \cdot 10^{-1}$

Table 7 Spectral decomposition results

5.2 k_{def} interpretation

By analogy with the bending creep of beams, the deferred displacement of the column head u_{fin} can be expressed as follows:

$$u_{fin} = u_{G,inst} \cdot \left(1 + k_{def}\right) + \sum_{n=1}^{4} u_{Qn,inst} \cdot \left(1 + \psi_{2,n} \cdot k_{def}\right) \quad (14)$$

where: $u_{G,inst}$ denotes the instantaneous displacement induced by the permanent loads; $u_{Q_n,inst}$ the instantaneous displacement induced by the operating loadings characterized by their loading time t_n ; k_{def} the long-term creep amplification; and parameter $\psi_{2,n}$ a moderation of the creep effects, as a function of the loading duration characterized by t_n ($n \in [1,...,4]$) [16]. By combining the time evolution of the creep function (Eq. (11)) with the definition of differed displacement at the column head, k_{def} and $\psi_{2,m}$ can be defined as follows:

$$k_{def} = \sum_{m=1}^{4} \chi_m \cdot \left(1 - \exp^{-\frac{t_4}{\tau_m}}\right) \quad (15)$$

$$\psi_{2,n} = \frac{\sum_{m=1}^{4} \chi_m \cdot \left(1 - \exp^{-\frac{t_n}{\tau_m}}\right)}{k_{def}} \quad (16)$$

By applying these expressions to the experimental values listed in Table 6, we obtain, for the five tested columns, the long-term properties presented in Table 8.

	Column 1	*Column 2*	*Column 3*	*Column 4*	*Column 5*	*Average value / Standard deviation*	*Eurocodes 5 and 1*
k_{def}	0.16	0.29	0.27	0.28	0.28	0.28 / 1%	0.6
$\psi_{2,1}$	0.16	0.01	0.02	0.02	0.02	0.01 / 1%	0.0
$\psi_{2,2}$	0.39	0.32	0.36	0.31	0.27	0.31 / 4%	0.3
$\psi_{2,3}$	0.62	0.57	0.59	0.56	0.53	0.56 / 4%	0.6
$\psi_{2,4}$	1.0	1.0	1.0	1.0	1.0	1.0 / 0%	1.0

Table 8 Long-term experimental properties vs. Eurocode 5 and Eurocode 1 (Service class no. 1)

These results are completed by the values assumed in Eurocode 5 [7] and Eurocode 1 [16]. Results have been given herein for service class no. 1; they reveal an atypical behavior of column no. 1, which may be due to either a problem during the initial loading or a misinterpretation of the increase in moisture during the first 150 days (corresponding to the moisture equilibrium). For this reason, we propose discarding column no. 1 in the statistical processing of results.

Two major remarks can thus be deduced from this study. First, let's note that the k_{def} of the compressed elements is half that set for the flexural elements (i.e., 0.3 vs. 0.6). This first conclusion prompts us to consider a complement for Eurocode 5. Secondly, regarding the values of $\psi_{2,m}$, it is concluded that the values assigned in Eurocode 1 can be applied directly to the combinations of actions targeting compressed elements.

6. Conclusion and perspectives

This work has made it possible to define the long-term behavior of wood elements subjected to compressive loading. First, an experimental device was created to establish a mechanical state of creep by limiting the stresses to a service limit state, as defined in Eurocode 5. An experimental protocol was then proposed to isolate the effects of shrinkage and swelling that contribute to the mechanical response of timber elements subjected to a compressive state. During a second step, a spectral decomposition of the deferred behavior allowed accurately identifying the creep kinetics over an entire year of loading. Lastly, an extrapolation strategy was used to determine the creep function over 50 years, which correspond to the deferred effects of a permanent load. This work has allowed drawing a conclusion on the k_{def} coefficient to be considered for compressed elements by highlighting a value half that typically used for elements in bending.

In parallel, the intermediate creep effects led to the conclusion that the partial creep coefficients corresponding to each loading duration class were indeed well matched. The work program was exclusively limited to service class 1. Moreover, this work was limited to correcting the creep coefficient k_{def}. However, creep effects also cause an apparent decrease in mechanical strength through the coefficient k_{mod} at the ultimate limit state. A short-term perspective calls for developing this study in order to determine the k_{mod} coefficient, which moreover should exert a lesser impact on both the short- and long-term strength of compressed elements.

In conclusion, this study has highlighted the effects of shrinkage-swelling in combination with the effects of creep. Over the longer term, this effort will require deep reflection on the incorporation of hygrothermal conditions with respect to the displacement and stress response of elements in compression.

7. References

[1] Xu F., Xuan S., Li W., Gao Y., Compressive performance of steel-timber composite L-shaped columns under concentric loading, Journal of Building Engineering, 48, 2022, https://doi.org/10.1016/j.jobe.2021.103967.

[2] Kang S. B., Xiong G., Feng S; Y., Zhu H., Zhou S. R., Behaviour of glulam timber frames with different beam-column connections and braces under reversed cyclic loads, Journal of Building Engineering, 49, 2022, https://doi.org/10.1016/j.jobe.2022.104031.

[3] O'Callaghan R.B., Lacroix D., Kim K.E., Experimental investigation of the compressive behaviour of GFRP wrapped spruce-pine-fir square timber columns, Engineering Structures, 252, 2022, https://doi.org/10.1016/j.engstruct.2021.113618.

[4] Lopez-Molina A., Doudak G., Retrofit techniques for Cross-Laminated Timber (CLT) elements subjected to blast loads, Engineering Structure, 197, 2019, https://doi.org/10.1016/j.engstruct.2019.109450.

[5] Zheng X., Li Z., He M., Lam F., Experimental investigation on the rheological behavior of timber in longitudinal and transverse compression, Construction and Building Materials 304, 2021, https://doi.org/10.1016/j.conbuildmat.2021.124633.

[6] Jockwer R., Grönquist P., Frangi A., Long-term deformation behaviour of timber columns : monitoring of a tall timber building in Switzerland, Engineering Structures, 2021, https://doi.org/10.1016/j.engstruct.2021.111855.

[7] Eurocode 5, Design of timber structures – Part 1-1 : General and rules for buildings. CEN. (EN 1995-1-1), 2010.

[8] Bazant, Z. P., Constitutive equation of wood at variable humidity and temperature, Wood Science and Technology, 19, 1985, pp.159-177.

[9]Dubois, F., Randriambololona, H., Petit, C., Creep in wood under variable conditions : Numerical modelling and experimental validation, Mechanics of Time Dependent Materials, 9, 2005, pp.173-202.

[10] Dubois F., Husson J. M., Sauvat N., Manfoumbi N., Modeling of the viscoelastic, mechano-sorptive behavior in wood, Mechanics of Time Dependent Materials, 16:4, 2012, pp. 439-460, https://doi.org/10.1007/s11043-012-9171-3.

[11] Gräfe M., Dietsch P., Winter S. (2018), CLT under in-plane loads : Investigation on stress distribution and creep, Conference of the International Network on Timber Engineering Ressearch, Tallin, August 2018, Estonia.

[12] Mirko Massaro F., Arne malo K., Long-term behaviour of Norway spruce glulam loaded perpendicular to grain, European Journal of Wood and Wood Products, 77, 2019, pp.821-832, https://doi.org/10.1007/s00107-019-01437-4.

[13] Manfoumbi N., Sauvat N., Dubois F., Découplage expérimental des déformations d'éléments bois sous chargements hydrique et mécanique variables. European Journal of Environmental and Civil Engineering 16, 2012, pp.1168-1186, https://doi.org/10.1080/19648189.2012.681941.

[14] Merakeb S., Dubois F., Petit C., Modeling of the sorption hysteresis for wood, Wood Science and Technology, 43, 2009, pp.575-589, https://doi.org/10.1007/s00226-009-0249-2.

[15]Varnier M., Sauvat N., Ulmet L., Montero C., Dubois, F., Gril, J., Influence of temperature in a mass transfer simulation: application to wood, Wood Science and Technology 54, 2020, pp.943-962, https://doi.org/10.1007/s00226-020-01197-y.

[16] Eurocode 1, Basis of design and actions on structures and National, Application document — Part 1 : Basis of design (ENV 1991-1), 1996, https://doi.org/10.5169/seals-56051.